

HIRIS Performance Study

John P. Kerekes and David A. Landgrebe

Laboratory for Applications of Remote Sensing
and School of Electrical Engineering,
Purdue University,
West Lafayette, IN

1. Introduction

In this report, the remote sensing system simulation is used to study a proposed sensor concept. An overview of the instrument and its parameters is presented, along with the model of the instrument as implemented in the simulation. Signal-to-noise levels of the instrument under a variety of system configurations are presented and discussed. Classification performance under these varying configurations is also shown, along with relationships between signal-to-noise ratios, feature selection, and classification performance.

2. Instrument Description

Driven by the recent advances in optical detector array technology and the opportunities for a permanent polar orbiting platform provided by the upcoming space station program, research and development has been progressing on a High Resolution Imaging Spectrometer (HIRIS) [1]. This instrument is planned to be a part of a cluster of scientific instruments forming the Earth Observing System (EOS) to be launched in the mid 1990's. This international group of instruments will provide many new forms of scientific data of the Earth's surface & atmosphere.

The HIRIS instrument will provide high spectral resolution samples across the visible and near infrared portions of the optical spectrum by the use of large CCD infrared detector arrays. The incoming radiance will be spectrally dispersed onto the arrays to provide one line of spatial data in each of the spectral bands simultaneously, as shown in Figure 1. The two dimensional image is then formed by the forward motion of the instrument platform.

In the proposed instrument there will be two separate detector arrays to cover the entire spectral range. The Very Near InfraRed (VNIR) array will provide 64 bands between 0.4 and 1.0 μm , while the Short Wave InfraRed (SWIR) array will contain 128 bands from 1.0 to 2.5 μm .

Functional parameters of the instrument are summarized in Table 1. One particular item of note is that the maximum output data rate is smaller than the internal data rate, thereby necessitating data editing or compression be performed on board the instrument.

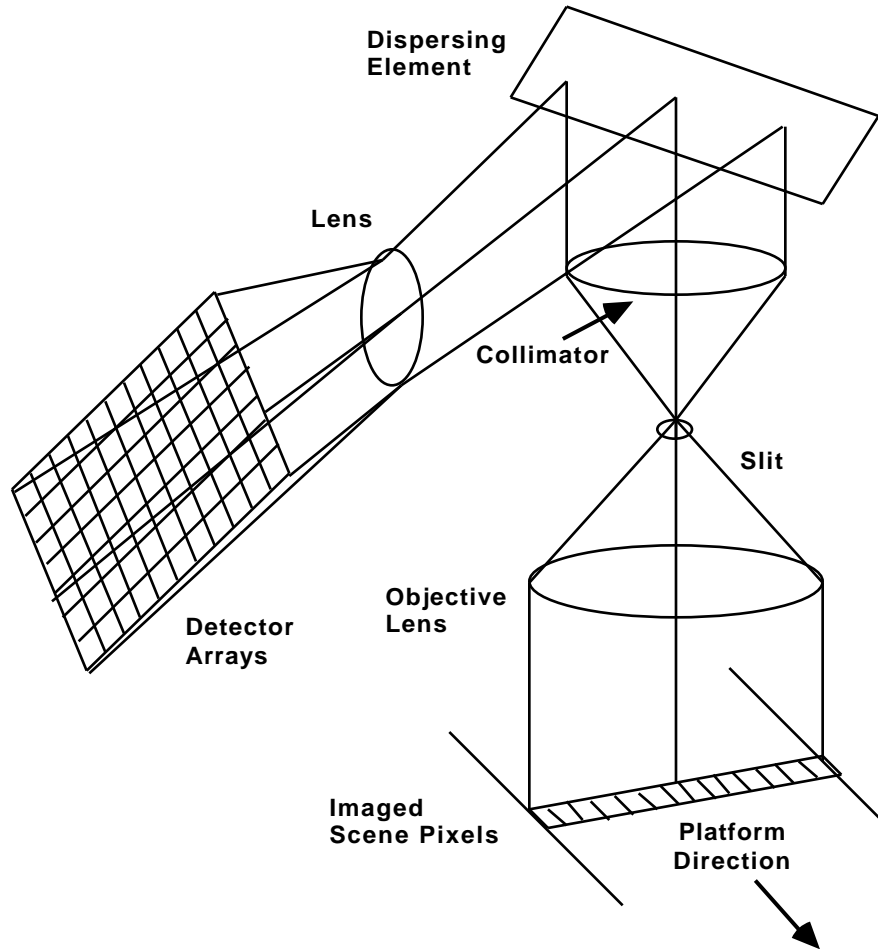


Figure 1. Imaging Spectrometer Configuration

Design Altitude	705 Km
Ground IFOV	30 m
Swath Width	20 Km
Spectral Coverage	0.4 - 2.5 μm
	192 Bands
Average Spectral Sample Interval	
0.4 - 1.0 μm	9.4 nm
1.0 - 2.5 μm	11.7 nm
Pointing	
Down-track	+60 $^{\circ}$ /-30 $^{\circ}$
Cross-track	+20 $^{\circ}$ /-20 $^{\circ}$
Data Encoding	12 bits/pixel
Maximum Internal Data Rate	512 MBPS
Maximum Output Data Rate	300 MBPS
Image Motion Compensation Gain	1, 2, 4, or 8

Table 1. HIRIS Functional Parameters

This instrument will be operated in an on-demand mode by gathering data only at the request of a scientific investigator. As part of that request, the investigator will need to specify several mission parameters. A typical list is given in Table 2. The goal of this report is to investigate sensor performance under a variety of mission parameter settings.

Location of Observation Site on Earth
Time of Day/Year or
Zenith Angle of Sun
Relative Azimuth between Sun and HIRIS
Look Angle of HIRIS
Acceptable Atmospheric Quality
IMC Gain State
Radiometric Resolution
Spatial Data Editing/Compression
Spectral Data Editing/Compression

Table 2. Example HIRIS Mission Parameters

3. Instrument Model

For this investigation the model shown in Figure 2 is used for the HIRIS instrument. This model version has 201 equally spaced (10 nm intervals) bands from 0.4 to 2.4 μm and includes most major spectral, spatial, and radiometric effects of the instrument. The model was implemented in the system simulation program described in reference [2].

Instrument parameters have been obtained from a progress report by JPL (reference [3]). These parameter levels are based upon preliminary specifications and prototype testing.

The following paragraphs and figures detail the blocks in the overall diagram.

3.1 Optics. The spectral transmissivity of the instrument optics is shown in Figure 3. Note the low response at the spectral gap between the VNIR and the SWIR arrays at 1.0 μm .

The normalized spatial response of the optics and field stop is assumed to be similar to the that of the Landsat Thematic Mapper instrument, as they both have a GIFOV of 30 meters. Figure 4 shows the measured down scene and across scene normalized responses as a function of angular distance, taken from reference [4]. The data points shown are the discrete values used in the simulation. At the nominal altitude of the instrument, the distance on the ground between these data points is approximately 7 meters.

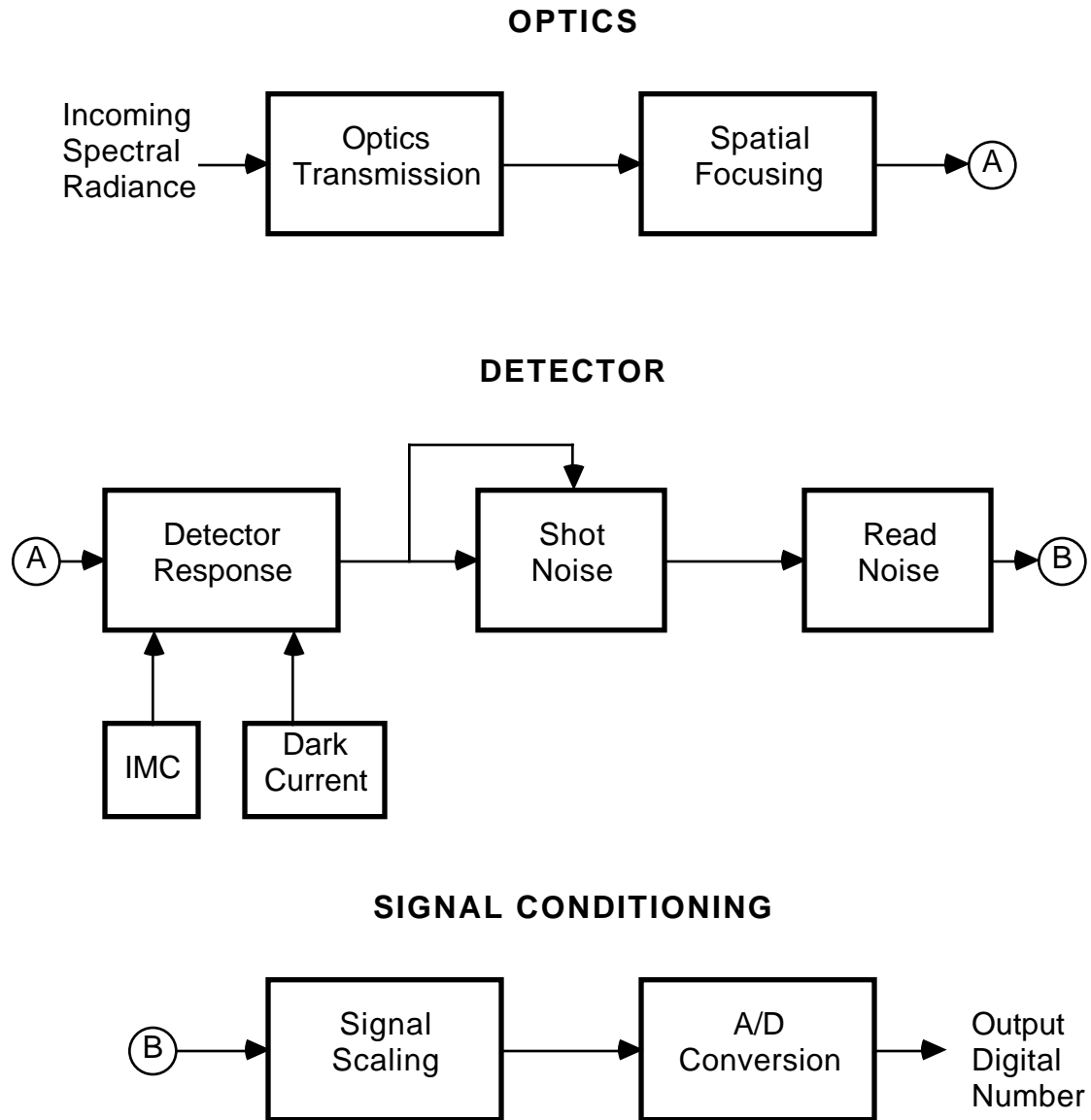


Figure 2. HIRIS Model Block Diagram

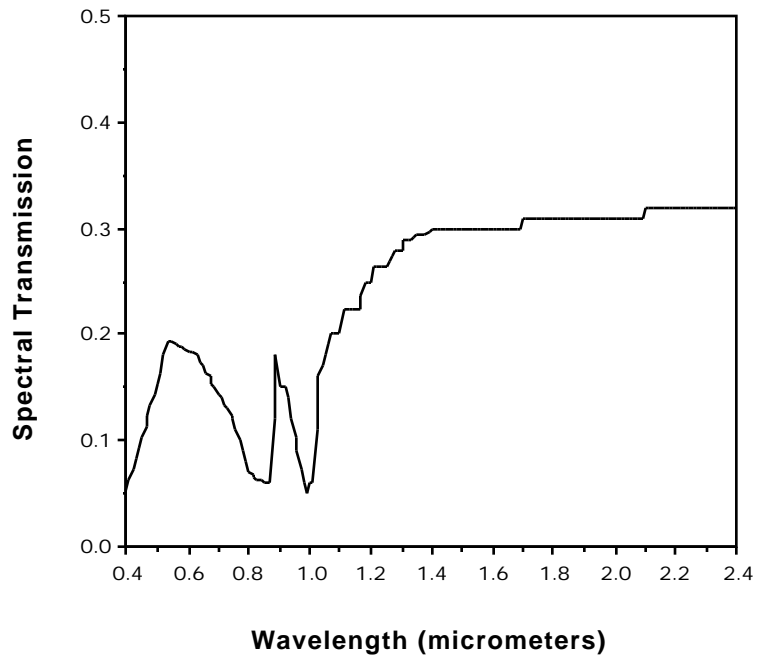


Figure 3. Spectral Transmissivity of Optics

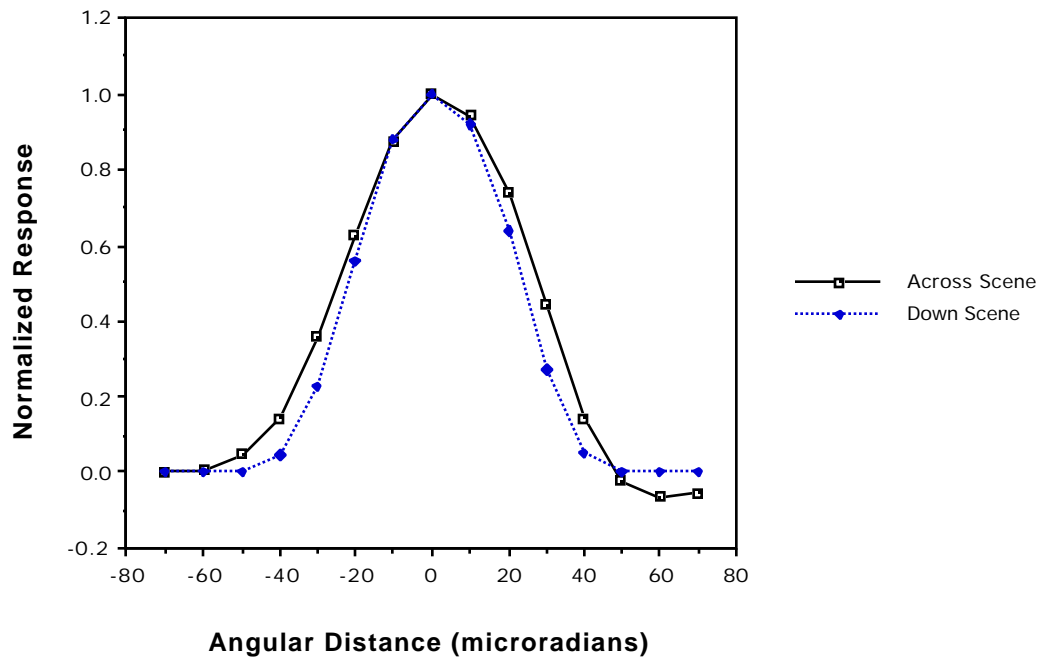


Figure 4. Normalized Spatial Response

The radiometric conversion from the incoming spectral radiance (mW/cm²-sr-μm) is accomplished by dividing by 1000 mW/W, and multiplying by the A , the product of the detector area and the solid angle of view, of the optics. The output of the optics model P , the incident spectral power, is then in units of watts/μm. The A used in the model is

$$A = 1.44 \times 10^{-6} \text{ cm}^2\text{-sr.}$$

3.2 Detector. The spectral quantum efficiency of the detectors is shown in Figure 5. The incident spectral power P at wavelength is converted to a number of electrons S at the detector by the integration of the incident photon level over the pixel integration time, as in equation (1).

$$S = P \cdot \Delta\lambda \cdot \frac{t}{hc} \quad (1)$$

where,

$\Delta\lambda$ = 10 nm, wavelength interval of spectral samples

λ = wavelength of interest (μm)

$h = 6.62 \times 10^{-34}$ Joule-sec, Planck's constant

$c = 3 \times 10^8$ meters/sec, the speed of light

$t = 4.5$ millisec, pixel integration time

Since the noise level data and full scale specifications were obtained in terms of number of electrons, the signal level is stated in these same terms and is unitless.

The Image Motion Compensation (IMC) is implemented through movement of the down-track pointing mirror to offset the platform speed and effectively multiply the pixel integration time by the gain state selected: 2, 4, or 8.

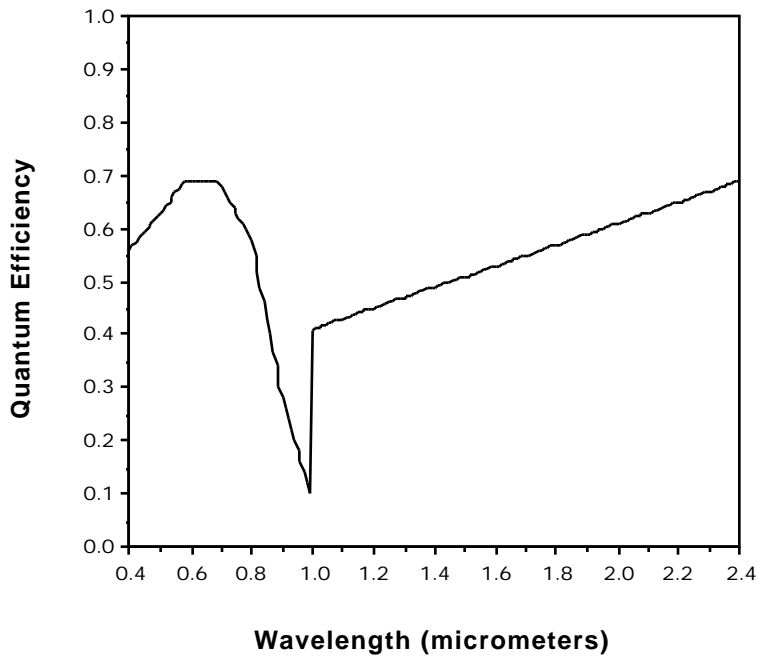


Figure 5. Spectral Quantum Efficiency

3.3 Noise. The noise in this model consists of a deterministic dark signal level, and random shot and read noise. Thermal noise has been found to be insignificant. All noise is considered to be stochastically independent between noise types and spectral bands. While calibration errors are expected to be significant, data have not been obtained to develop an appropriate model. Thus, this type of error has not been included as of yet.

The dark current level is given in Table 3. This level is added to the total received signal.

VNIR	0 e ⁻
SWIR	2.7 x 10 ⁴ e ⁻

Table 3. Dark current levels in terms of electrons

The shot noise in the model consists of zero mean Gaussian random numbers with a standard deviation equal to a function of the total signal level in the detectors. This total signal is comprised of the incoming radiance, and the dark current level mentioned above. Figure 6 shows several points relating total signal and shot noise levels, along with a best fit curve and its equation.

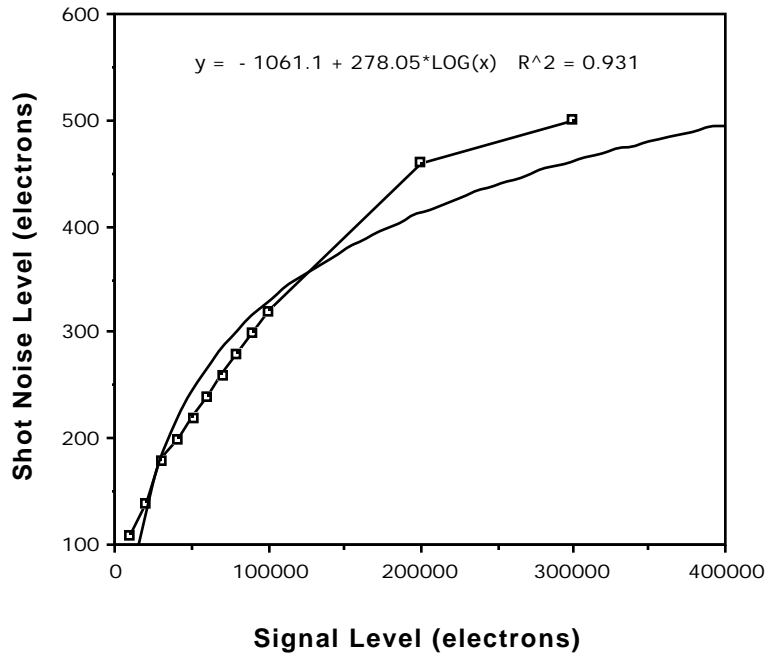


Figure 6. Shot Noise vs. Signal Level

Thus, the standard deviation of the shot noise process is given by equation (2).

$$\text{shot} = -1060 + 278 \log_{10} S' \quad (2)$$

S' is the total detector signal level in electrons. Note, this relationship is assumed to be independent of wavelength.

Read noise is added in as a zero mean Gaussian random number with a standard deviation as in Table 4. Within each detector array, the read noise level is assumed to be constant over wavelength.

VNIR	300 e ⁻
SWIR	1000 e ⁻

Table 4. Read Noise Levels

3.4 Signal Conditioning. Table 5 gives the full scale e⁻ values F for each detector array. These are values obtained from the JPL report, and as with all of the data values presented, should be considered to be subject to change.

VNIR	577,395 e ⁻
SWIR	1,441,440 e ⁻

Table 5. Full Scale Electron Levels F

The conversion from the e⁻ levels S'' (received signal plus noise) to a digital number (DN) occurs as in equation (3).

$$DN = \text{nint} \frac{S''}{IMC \cdot F} \cdot 2^Q - 1 \quad (3)$$

where,

IMC = IMC Gain State

F = Full Scale Electron Level

Q = Number of radiometric bits (nominally 12)

The division by the IMC gain state is included to preserve the dynamic range of the detectors over the various gain states.

4. Signal to Noise Variations

This section presents the results of the effect of varying system parameters on the signal-to-noise ratio (SNR) of the HIRIS model.

In many Earth resource analysis remote sensing applications, the output product is some form of classification map of the observed area. The classification is usually obtained by a computer algorithm that uses the mean and covariances of the multispectral image data to distinguish between the classes. Thus, in this application, not only are signal levels important, but so are signal power variations.

To gain a more realistic sense of how the system parameters affect HIRIS performance, two versions of SNR are defined: Voltage SNR, and Power SNR. These are defined for each spectral wavelength band m as in equations (4) and (5).

$$\text{Voltage SNR}_m = 20 \log_{10} \frac{\overline{m} G_m}{\sqrt{2_{\text{shot},m}^2 + 2_{\text{read},m}^2 + 2_{\text{quant}}^2}} \quad (4)$$

$$\text{Power SNR}_m = 10 \log_{10} \frac{2_{\text{shot},m}^2 + 2_{\text{read},m}^2 + 2_{\text{quant}}^2}{\overline{m}^2 G_m^2} \quad (5)$$

where,

\overline{m} = Mean surface reflectance at wavelength band m

- σ_m^2 = Variance of surface reflectance at wavelength band m
- G_m = Conversion factor with units of number of electrons due to the solar irradiance at the surface, atmospheric transmittance, and the sensor response for wavelength band m
- $\sigma_{\text{shot},m}^2$ = Variance of shot noise in wavelength band m
- $\sigma_{\text{read},m}^2$ = Variance of read noise in wavelength band m
- σ_{quant}^2 = Variance of quantization noise

The quantization noise is assumed to be uniform with a standard deviation of

$$\sigma_{\text{quant}} = \sqrt{\frac{2}{12}}$$

where σ_{quant} is the number of electrons per digitization interval.

For 12 bit radiometric resolution and the full scale values in Table 5, the standard deviation of the quantization error is given in Table 6.

VNIR	41 e ⁻
SWIR	102 e ⁻

Table 6. Standard Deviations of Quantization Error

For the SNR results included in this report, the system configuration shown in Table 7 was used as a baseline. The solar illumination and atmospheric effects were obtained using the LOWTRAN 7 [5] computer code. The 1976 U.S. Standard Atmosphere with rural extinction was used.

Meteorological Range	16 Km
Solar Zenith Angle	30°
Solar Azimuth Angle	180°
View Zenith Angle	0°
View Azimuth Angle	0°
IMC Gain State	1
Sensor Noise Levels	Nominal
Radiometric Resolution	12 bits

Table 7. Baseline System Configuration for SNR Study

Figure 7 shows the voltage SNR for three surface albedos and the baseline system configuration of Table 7.

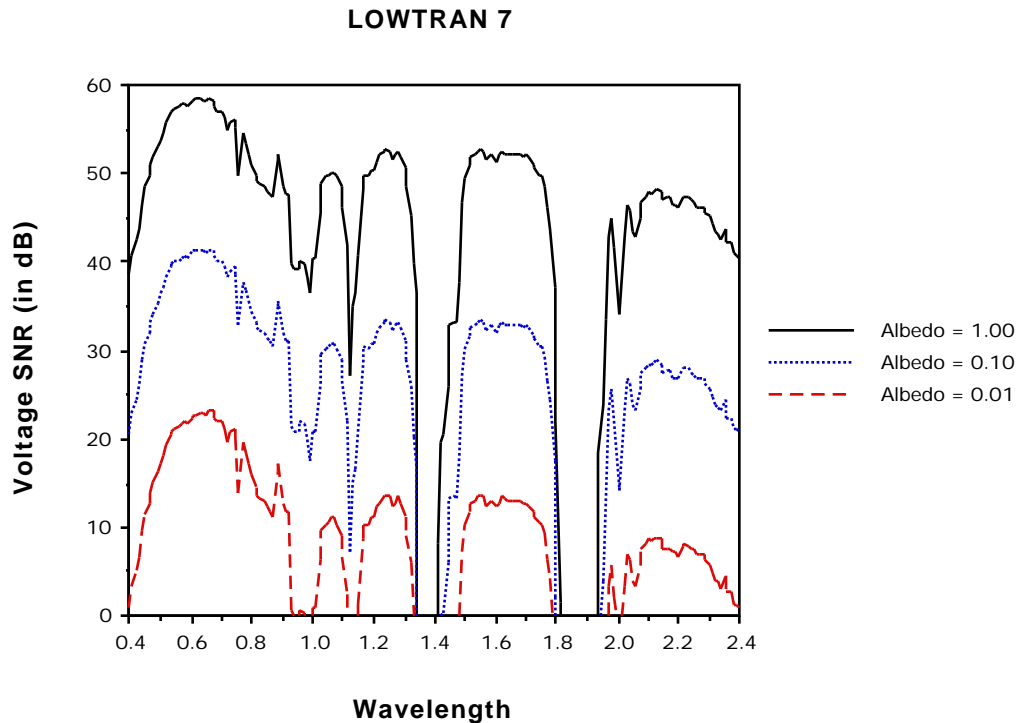


Figure 7. SNR of HIRIS for various albedos using LOWTRAN 7 and the baseline system configuration given in Table 7.

For the study of parameter effects on SNR, it was decided to use typical surface reflectance statistics rather than a deterministic albedo. The surface reflectance statistics used were obtained from a site in Finney County, KS on May 3, 1977 [6]. 1551 observations were combined from three classes: winter wheat, summer fallow, and an unknown class. The mean reflectance and variation of this data ensemble are plotted in Figure 8.

To obtain an idea of how this reflectance is modified by the atmosphere and sensor response, a simulated image was created using the baseline system configuration and the reflectance of Figure 8. The resulting mean digital counts and their variation are shown in Figure 9. Several effects are immediately noticeable. The absorption bands of the atmosphere are present, as well as a reversal in the relative values of the visible and infrared responses due to the solar illumination and gain settings of the sensor. Also, an apparent reduction in relative variation is seen due to the additive constant path radiance and dark current in the instrument. No correction for these effects was made.

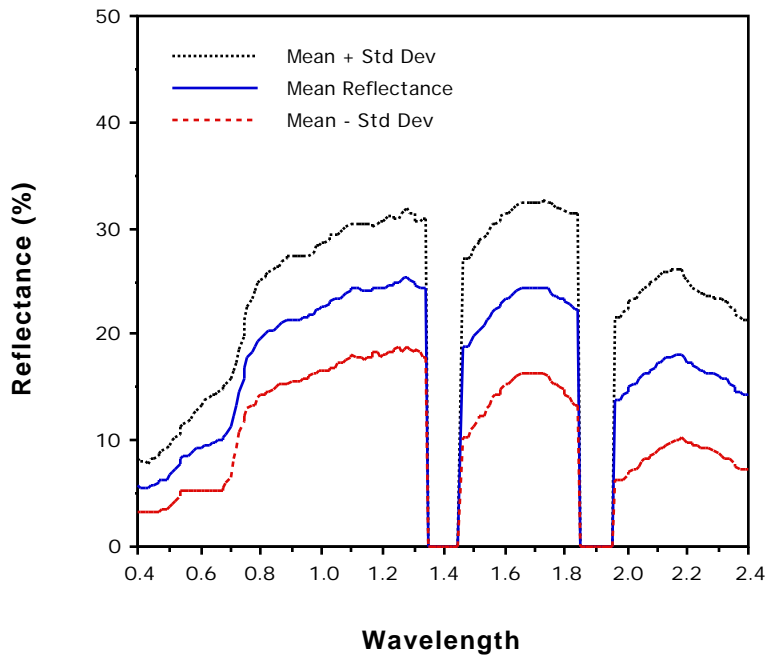


Figure 8. Mean and variation of the surface reflectance of the combined data set.

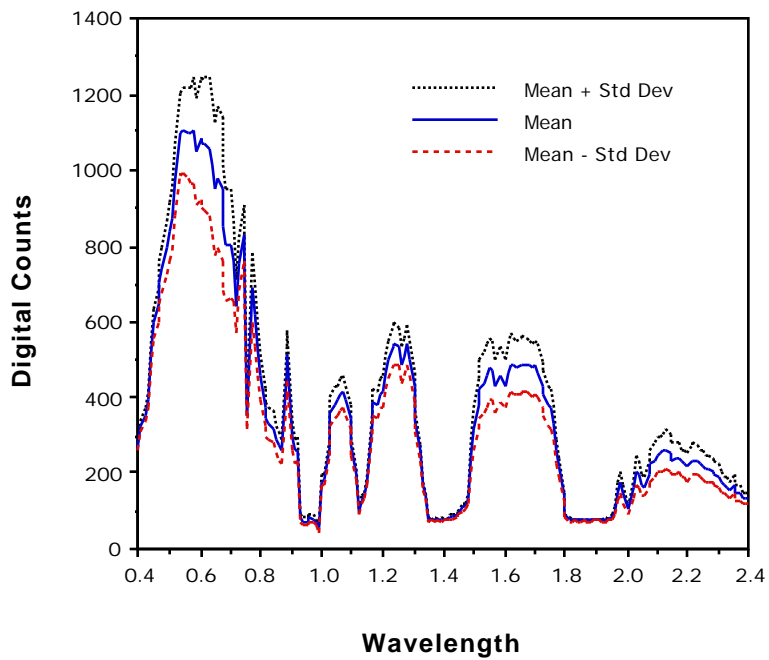


Figure 9. Mean and variation of image vector as received by HIRIS.

The following Figures 10 through 21 show the Voltage and Power SNR variations as a function of the parameters shown in Table 8.

Meteorological Range	2,4,8,16,32 Km
Solar Zenith Angle	0°, 15°, 30°, 45°, 60°
View Zenith Angle	0°, 15°, 30°, 45°, 60°
IMC Gain State	1, 2, 4, 8
Sensor Noise Levels	1/4, 1/2, 1, 2, 4
Radiometric Resolution	8, 10, 12, 14, 16 bits

Table 8. Parameters Studied and Their Variations

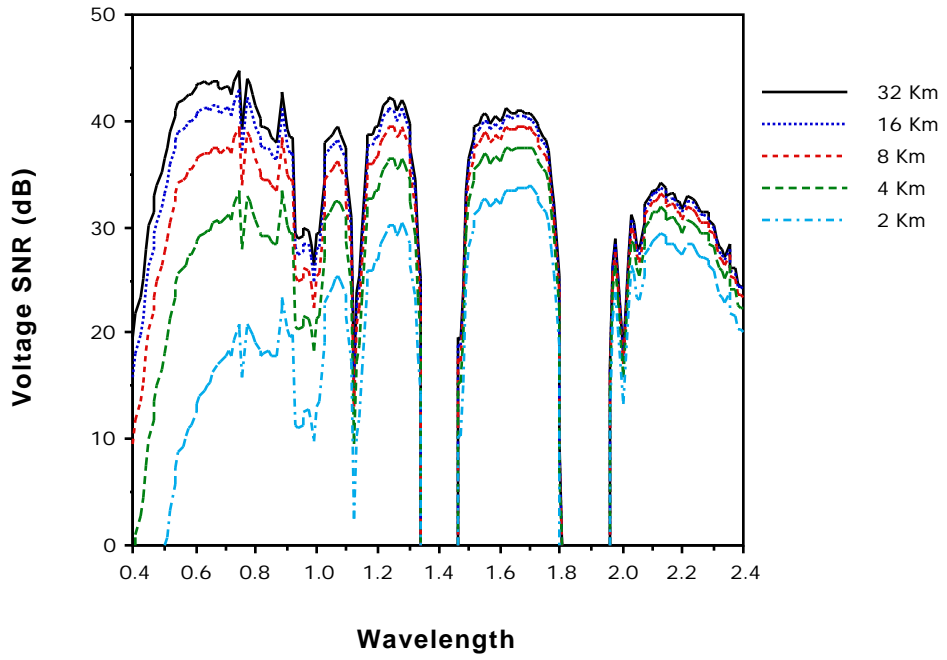


Figure 10. Voltage SNR for varying Meteorological ranges.

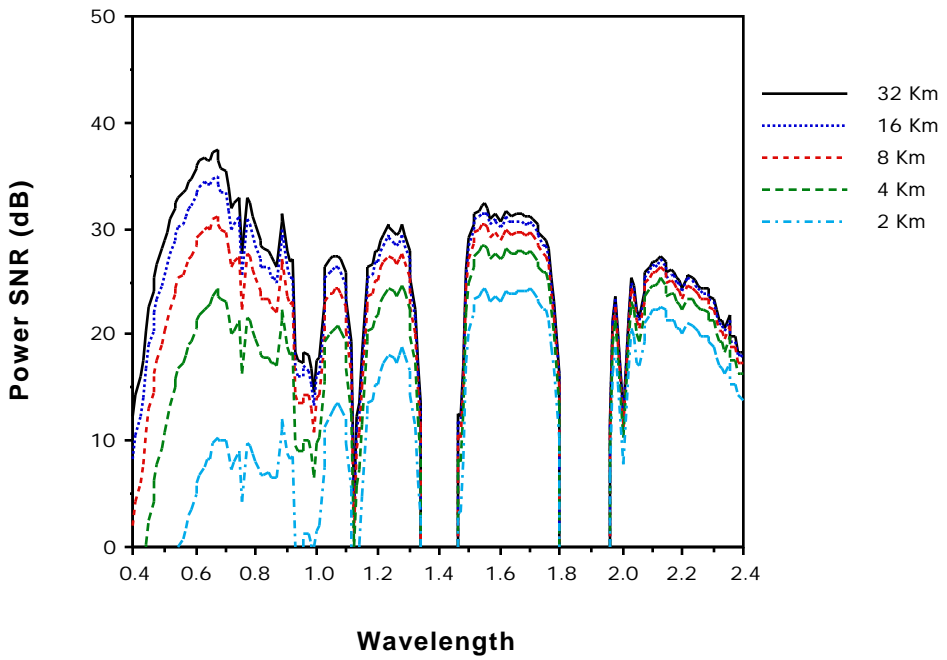


Figure 11. Power SNR for varying Meteorological ranges.

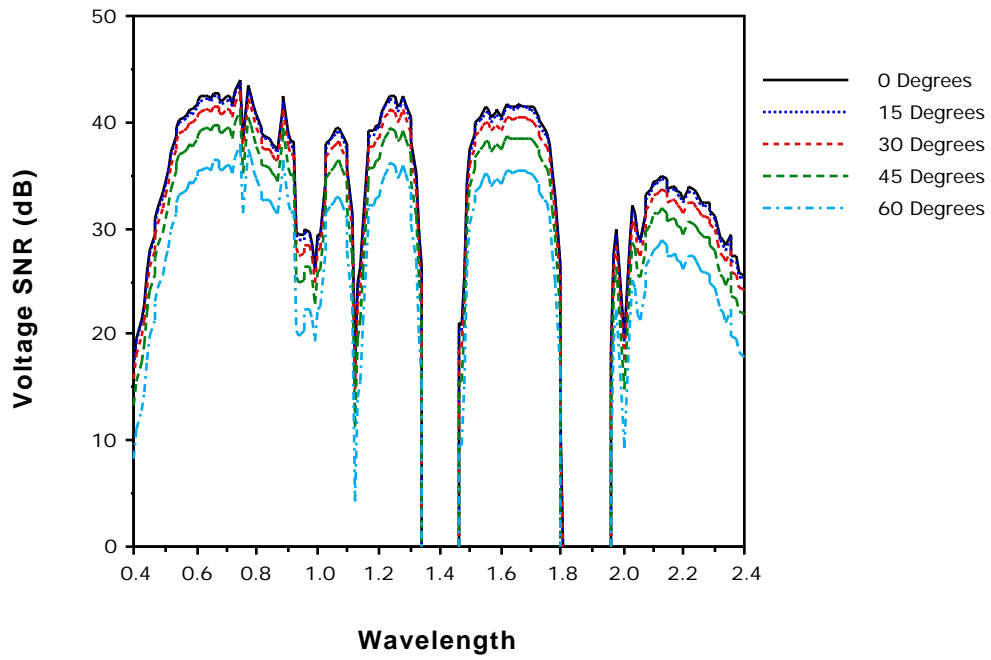


Figure 12. Voltage SNR for varying solar zenith angles.

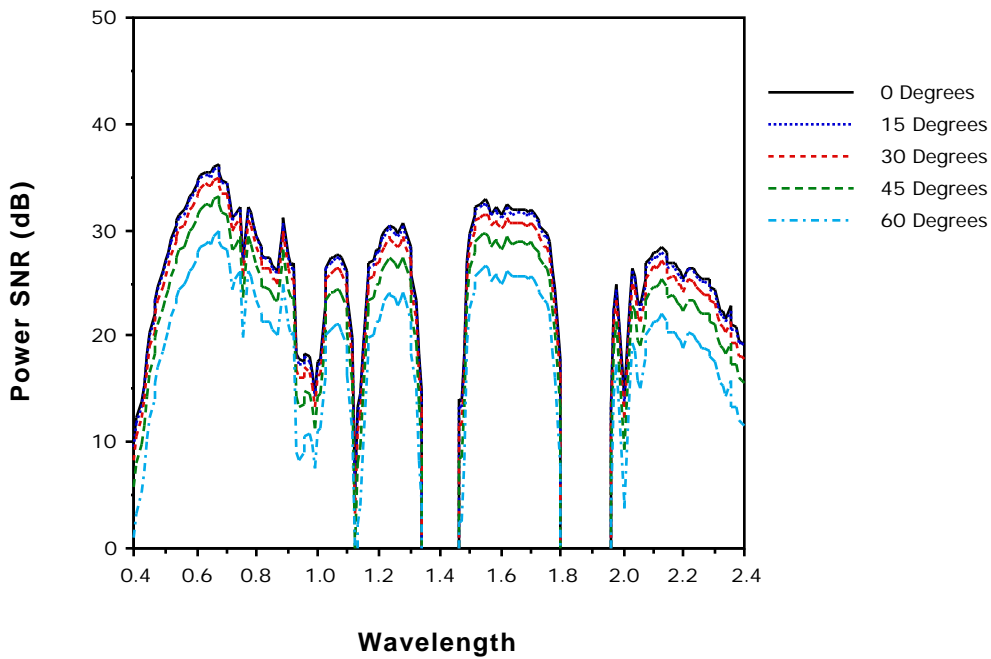


Figure 13. Power SNR for varying solar zenith angles.

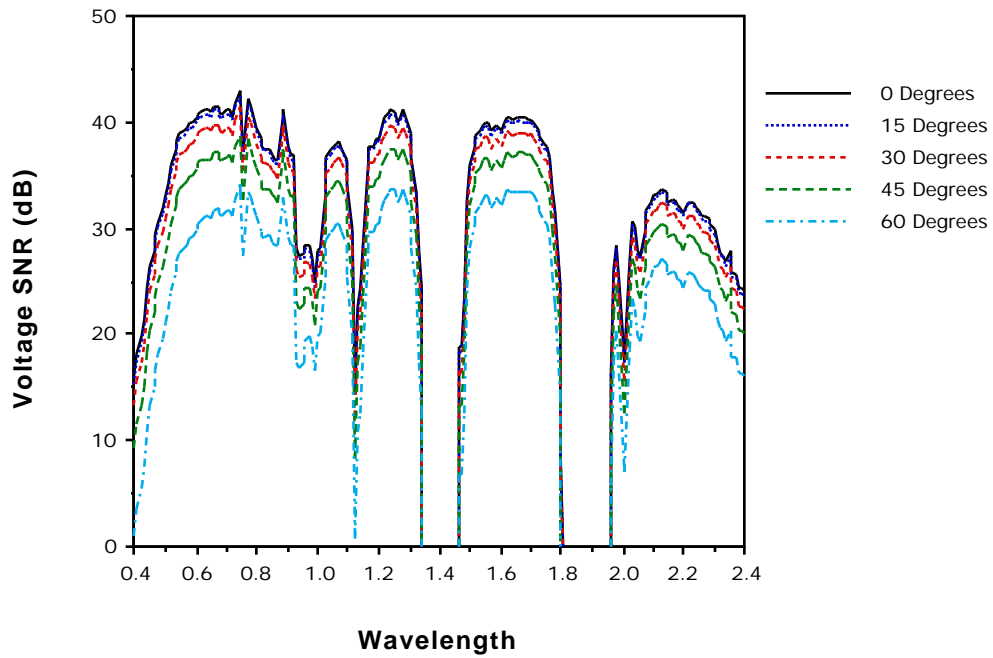


Figure 14. Voltage SNR for varying view zenith angles.

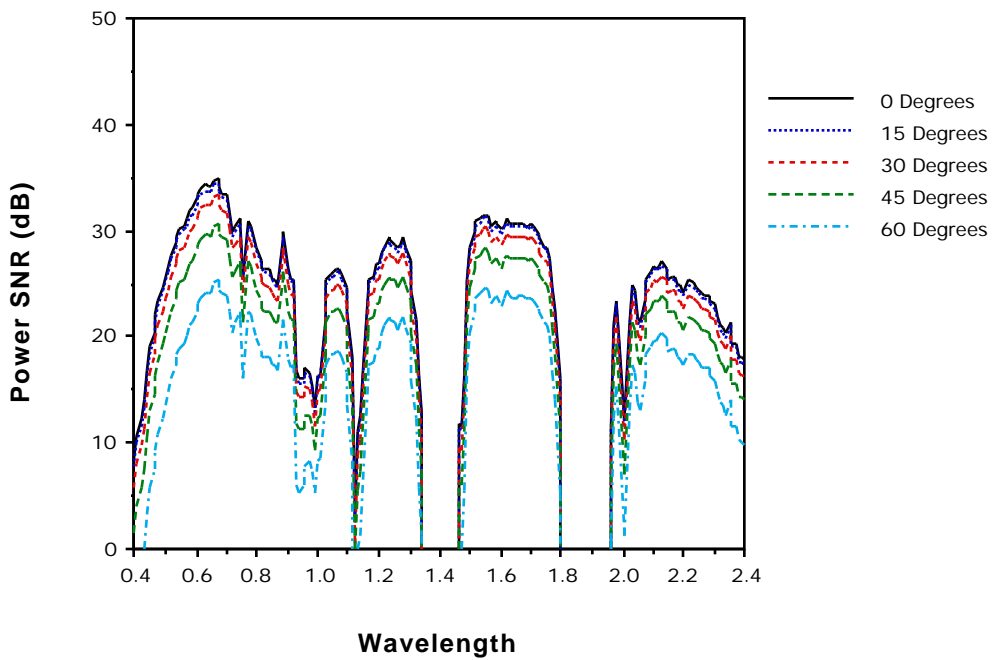


Figure 15. Power SNR for varying view zenith angles.

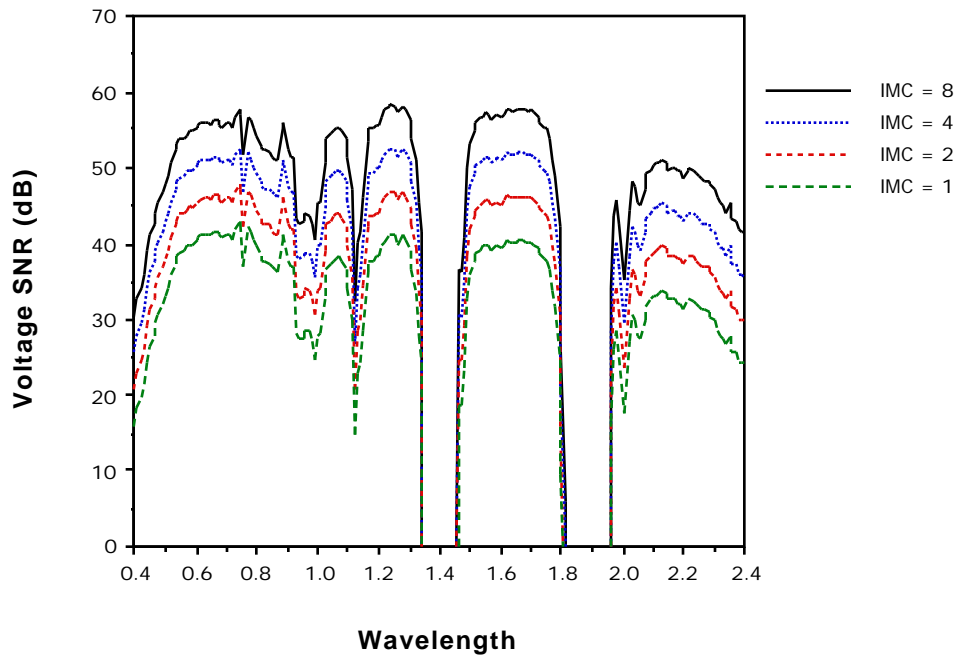


Figure 16. Voltage SNR for various IMC gain states.

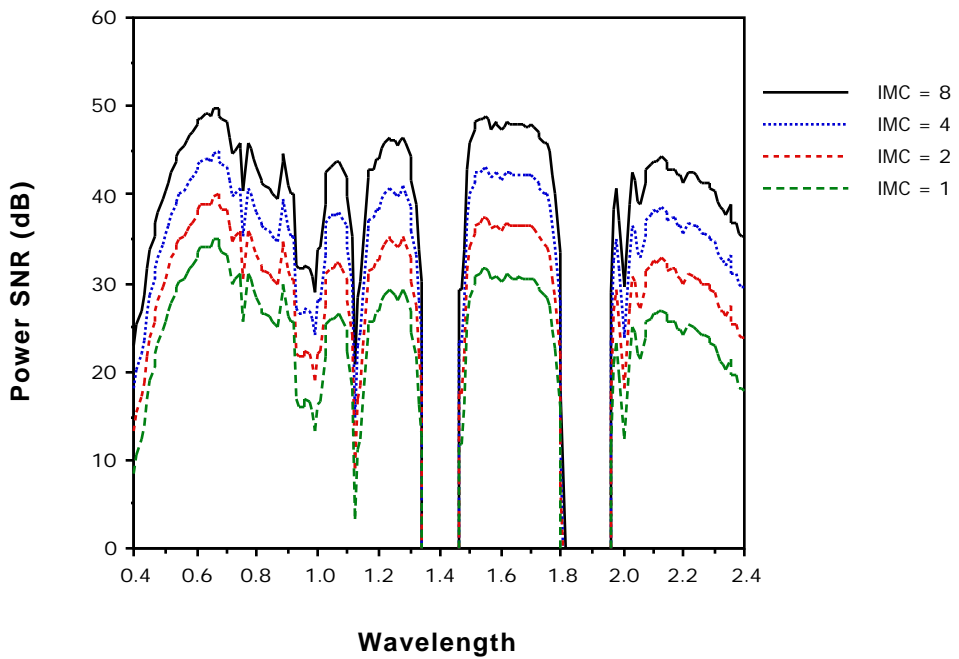


Figure 17. Power SNR for various IMC gain states.

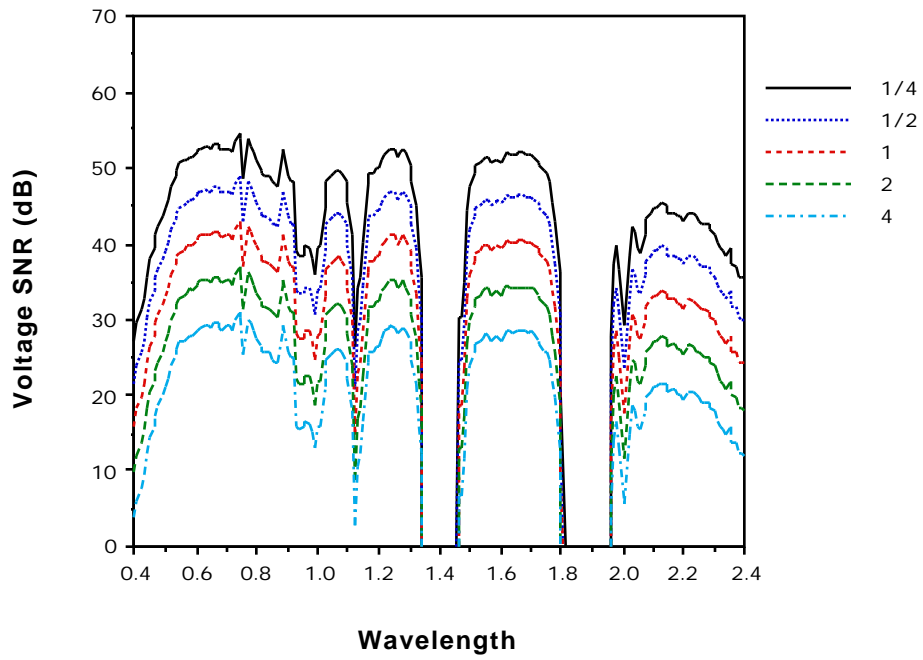


Figure 18. Voltage SNR for varying factors of shot and read noise.

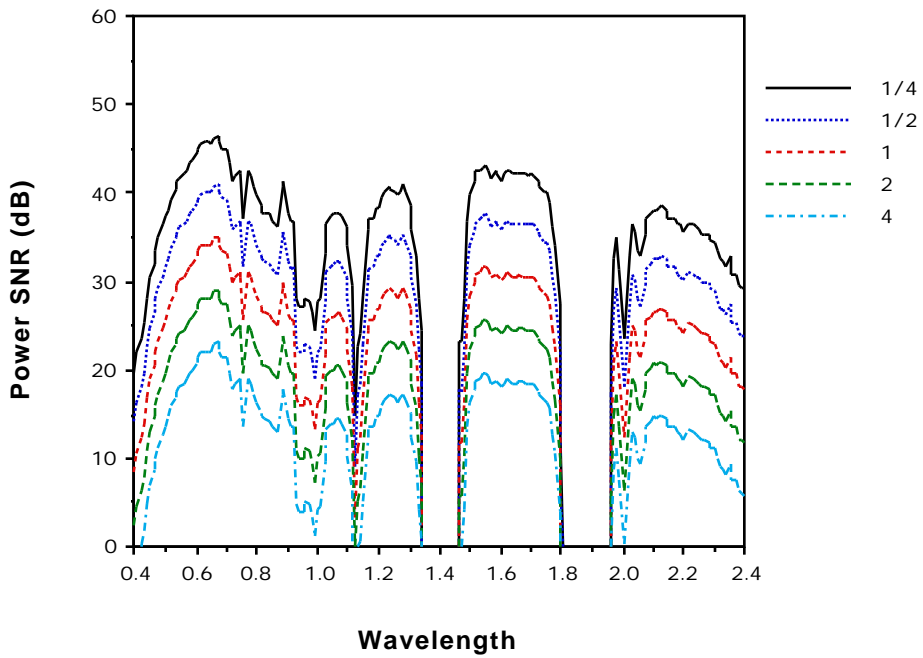


Figure 19. Power SNR for varying factors of shot and read noise.

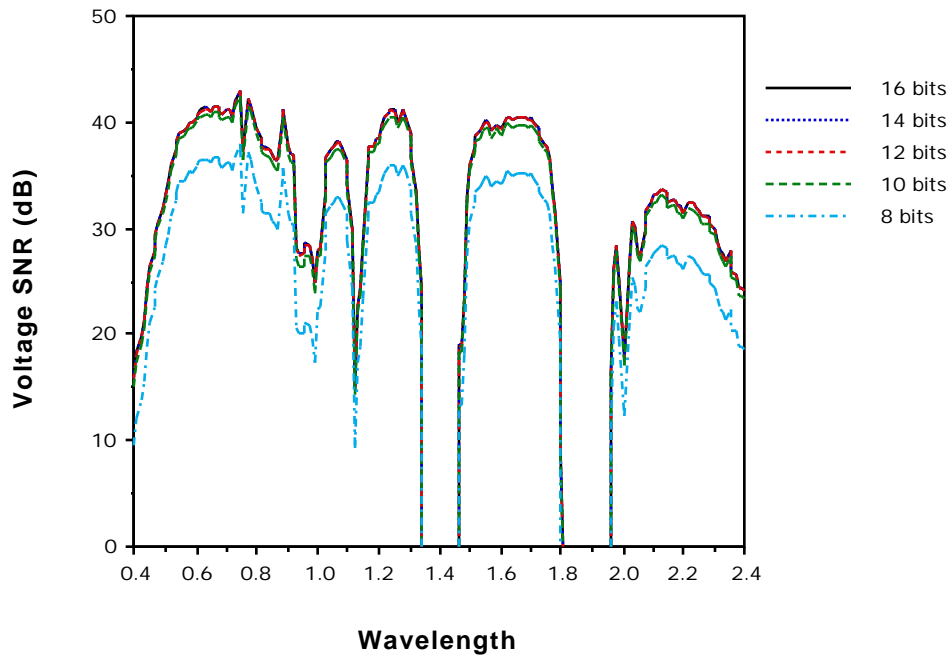


Figure 20. Voltage SNR for various numbers of bits.

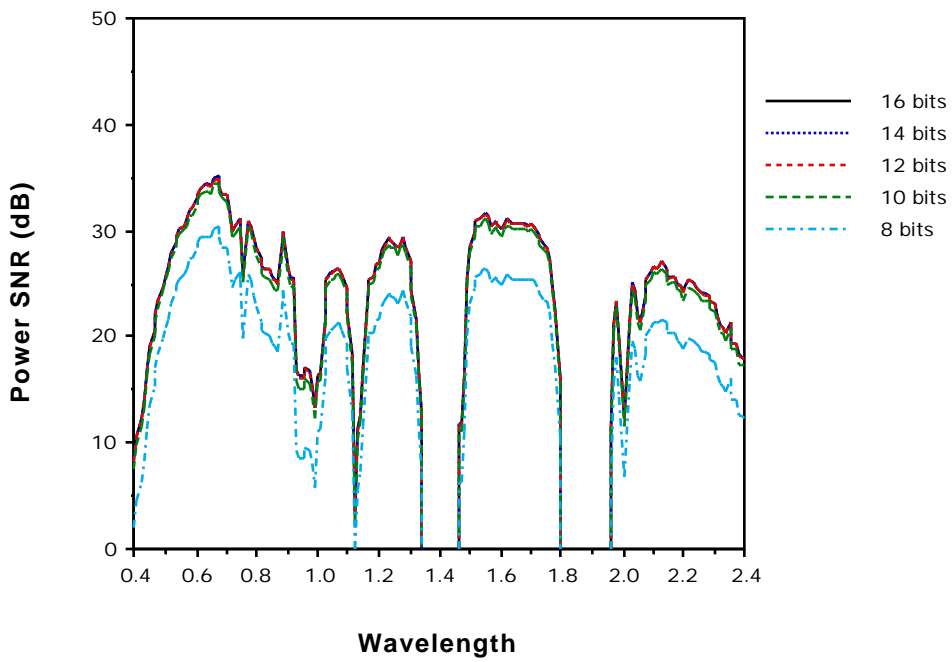


Figure 21. Power SNR for various numbers of bits.

Several common features of all the graphs are immediately noticeable. The wide water absorption bands are present at 1.4 and 1.9 μm , while several narrow absorption bands due to other atmospheric constituents are also present. The relatively low SNR's around 1.0 μm are due to the instrument optics and detector response fall off at the spectral gap between the VNIR and the SWIR arrays.

Looking at the effect of the meteorological range, one observes a more pronounced effect on the SNR in the visible and near infrared portions of the spectrum, than those at longer wavelengths.

Considering the goniometric configurations, the effects on SNR of varying the solar or view angle seem to be similar, at least for the system configuration chosen. Note that these variations here are only due to the atmospheric effect, as angle dependent reflectance variations of the surface were not considered in this model.

The effect of the IMC and noise level parameters seem to be reasonable and consistent. The radiometric resolution has little effect on SNR at resolutions of 12 bits or more. This seems to indicate that the quantization error at 12 or more bits is insignificant compared to other noise sources, while at 8 or 10 bits quantization error becomes the dominant noise source.

5. Parameter Effects on Classification Accuracy

The effects of the parameters in Table 8 were also studied on the classification performance of the HIRIS instrument. Simulated scenes were generated using the three classes of the Finney County data set of May 3, 1977 and the system simulation program [2]. Since the model HIRIS sensor generates images with 201 bands, a feature selection algorithm was applied that combines bands together to form each feature. For the following experiments, a set of 16 features were used with a maximum likelihood multivariate classifier (Gaussian assumption) to assess accuracy. Table 9 shows the wavelength bands combined for each of the features. These features are based upon the algorithm described in reference [7]. Table 10 contains relevant system parameters used in the simulation.

Feature	Wavelength (μm)
1	0.70 - 0.92
2	1.98 - 2.20
3	2.20 - 2.40
4	0.66 - 0.84
5	1.48 - 1.64
6	0.52 - 0.66
7	1.64 - 1.78
8	1.16 - 1.28
9	0.96 - 1.06
10	1.04 - 1.12
11	0.94 - 1.00
12	0.44 - 0.50
13	1.12 - 1.16
14	0.92 - 0.96
15	0.40 - 0.44
16	1.00 - 1.04

Table 9. Features used in classification experiments.

Scene Size	90 by 90 Pixels
Scene Pixel Size	15 meters
Image Size	45 by 45 Pixels
Number of Pixels per class	675
Number of training samples per class	300

Table 10. System Simulation Parameters.

The following Figures 22 through 27 show the results of the various parameter changes on classification accuracy. The accuracies shown are the average of the three class accuracies, and represent the mean of 10 repetitions of the simulator.

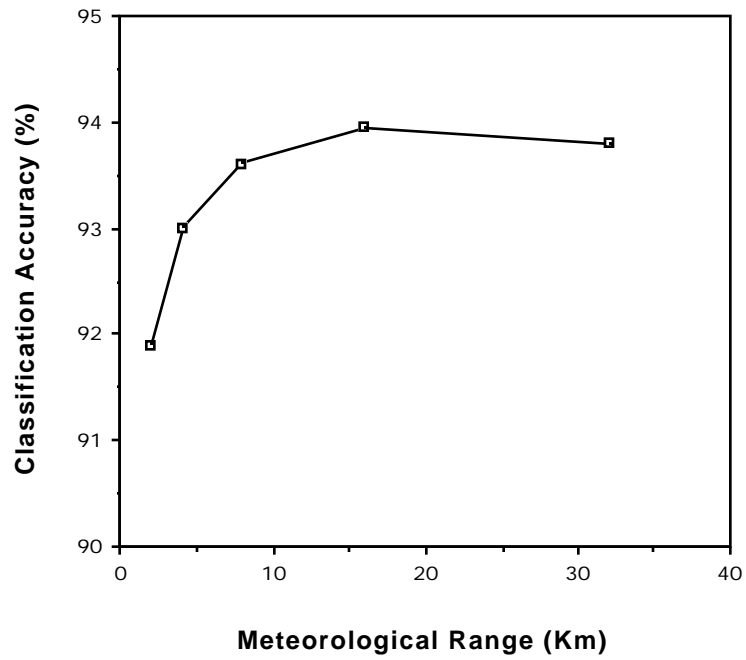


Figure 22. Classification accuracy vs. meteorological range.

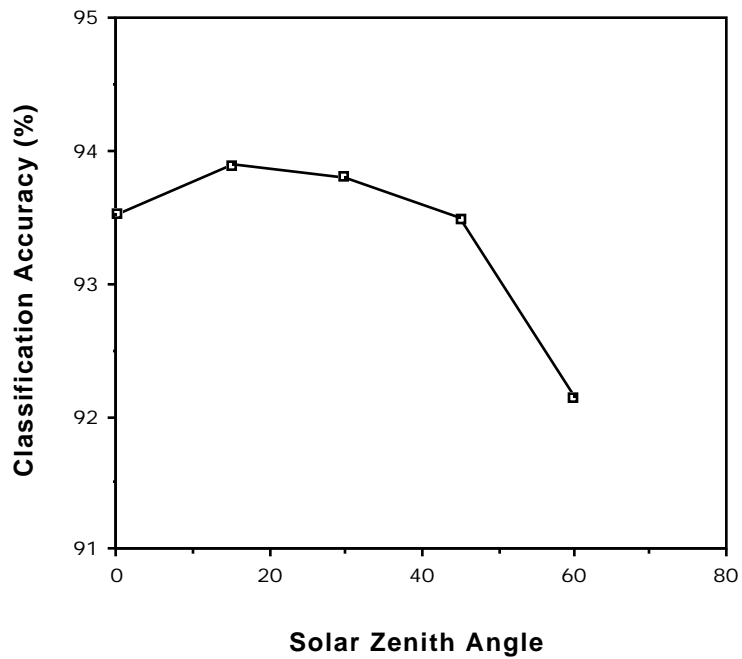


Figure 23. Classification accuracy vs. solar zenith angle.

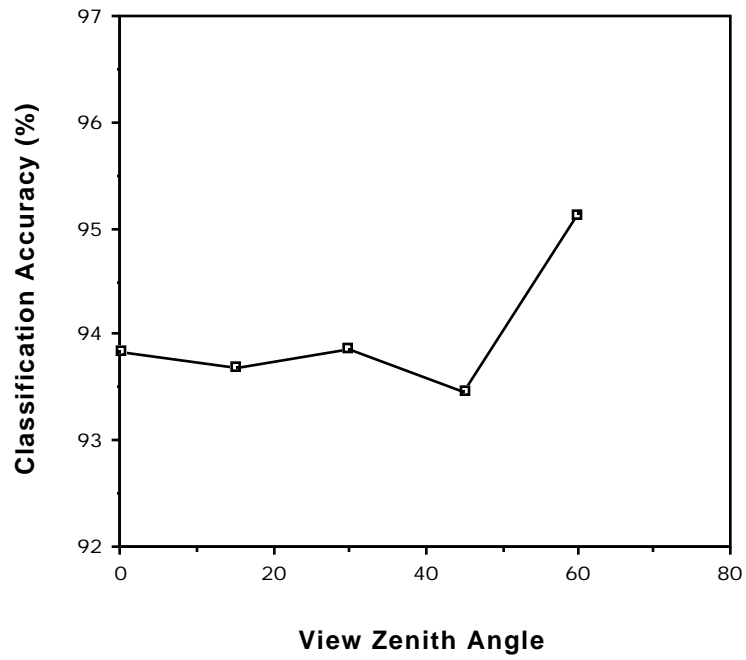


Figure 24. Classification accuracy vs. view zenith angle.

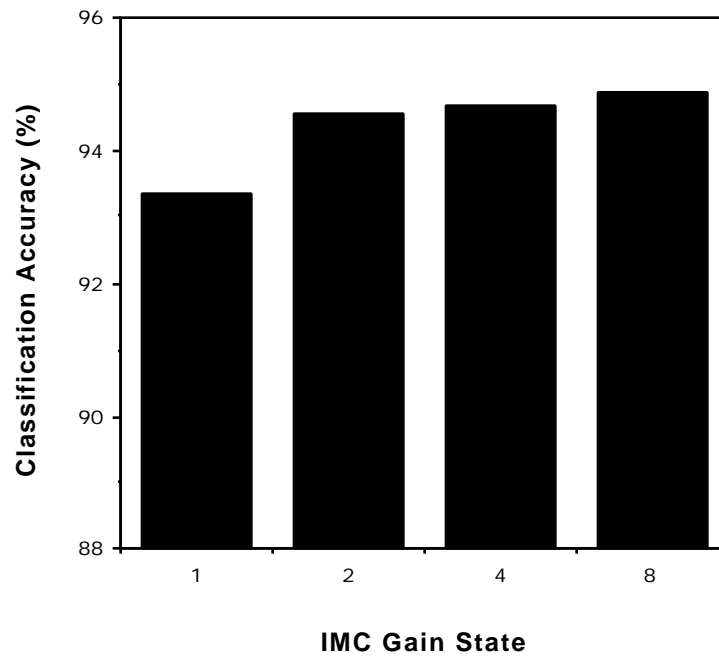


Figure 25. Classification Accuracy vs. IMC gain state.

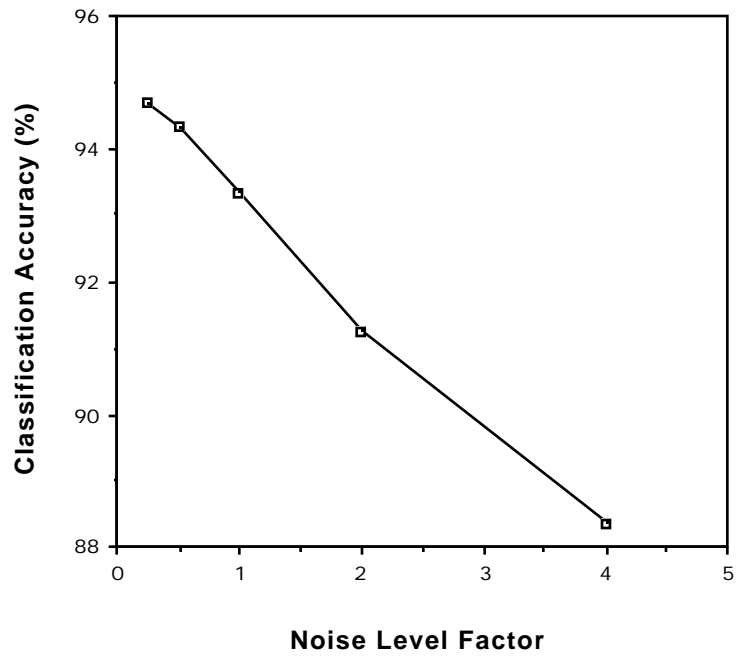


Figure 26. Classification Accuracy vs. shot and read noise level.

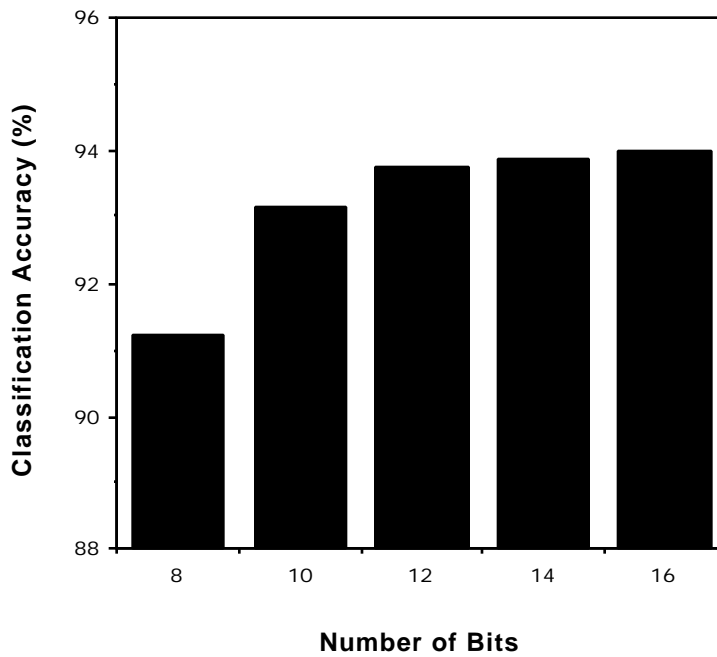


Figure 27. Classification Accuracy vs. number of bits.

Most of these results are as one would expect. In hazier atmospheres, or with high noise levels the accuracy decreases. Figure 24 showing the effect of view angle is a little less intuitively satisfying. The sudden rise in classification accuracy at a view angle of 60° is surprising. This seemingly abnormal result is due to the complex interaction of the scene pixel size and the sensor spatial response. At this view angle the distance on the ground between samples of the discrete spatial response becomes approximately 15 meters, the same as the size of the scene pixels. At angles less than 60° , about 25 scene pixels were appropriately weighted to form one image pixel. Now, at 60° , about 45 scene pixels are combined. This has the effect of reducing the within class variation and increasing the class separability and classification accuracy.

This result points out how complex interactions between components of the system can affect classification accuracy. It also points out some of the pitfalls in the use of a discrete simulation for the study of system effects. One must exercise caution in specifying system parameters and in interpretation of results.

One significant part of the real instrument not included in the model of Figure 2 is error in radiometric calibration. This omission is mainly due to the fact that adequate data does not exist to develop a model for this error. To test the significance of this omission, a model of the error based on percentage of value, and distributed uniformly with a mean of zero, was inserted before the signal conditioning. This error is distributed randomly across the image and represents a relative error. Figure 28 shows the effect of this error as it varies over the range of 0.0 to 4.0 percent.

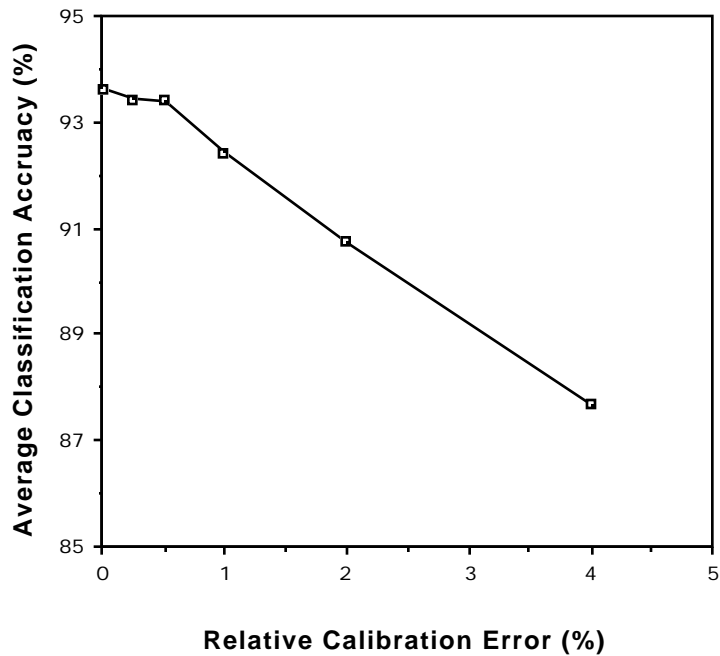


Figure 28. Accuracy vs. Relative Calibration Error

This model for calibration error shows a significant effect for errors on the order of one percent of value or greater, and shows the importance of accurate relative calibration.

Next, an experiment was run to evaluate the interrelationships of two parameters. The effect of the IMC gain state on classification accuracy vs. meteorological range was studied. Figure 29. shows the result. It appears that the IMC gain state has a greater effect on improving classification accuracy in hazy, or low meteorological range, atmospheres. But, even in clear atmospheres the higher gain state shows an improvement.

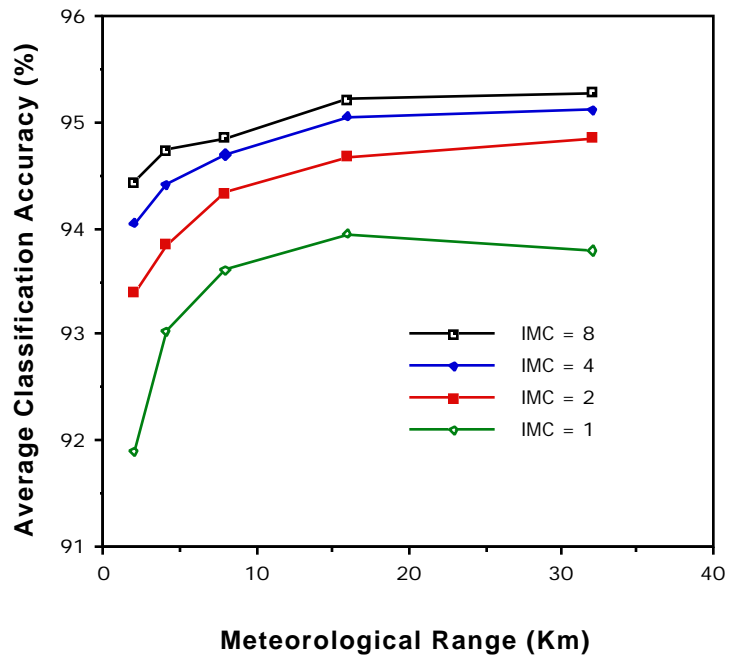


Figure 29. Classification accuracy vs. meteorological range for several IMC gain states.

6. Relationships between SNR, Classification Accuracy, Separability, and Feature Selection

In this section we discuss computing the SNR based on the combined features, and present results showing the relationships between this SNR, class separability and classification accuracy for several feature sets.

In calculating the SNR of a feature, the signal and noise levels of the L component wavelength bands are combined. In the case of the voltage SNR, the signal levels are simply added together, as are the variances of the noise levels. This is shown in equation 6.

$$\text{Feature Voltage SNR} = 20 \log_{10} \frac{\sum_{l=1}^L G_l}{\sqrt{\sum_{l=1}^L (\sigma_{\text{shot},l}^2 + \sigma_{\text{read},l}^2 + \sigma_{\text{quant},l}^2)}} \quad (6)$$

For the power SNR, the signal levels cannot be simply added because of the band-to-band correlation present in the reflectance data. Here, the signal variance is the sum of the individual variances, plus terms due to the covariance between each pair of bands l and m, combined in the feature as in equation (7).

$$\text{Feature Power SNR} = 10 \log_{10} \frac{\sum_{l=1}^L \sum_{m=1}^M G_l G_m}{\sum_{l=1}^L (\sigma_{\text{shot},l}^2 + \sigma_{\text{read},l}^2 + \sigma_{\text{quant},l}^2)} \quad (7)$$

An experiment was then carried out to determine if the SNR of a particular feature had any effect on its importance in classification. The combined voltage and power SNR's of the feature set shown in Table 9 were computed and the results shown in Figure 30.

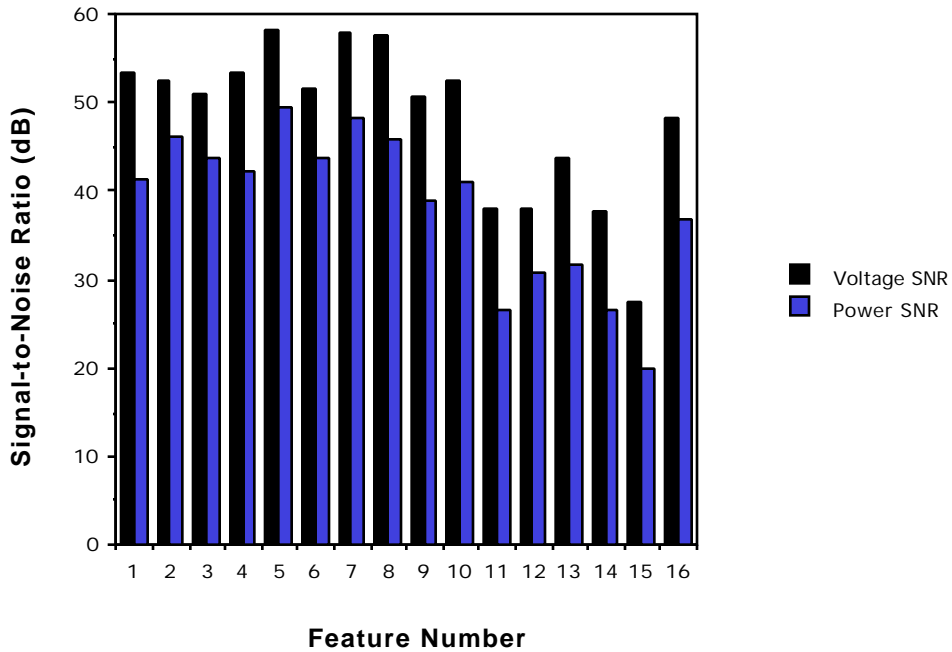


Figure 30. SNR's for features of Table 9.

These features were then ranked according to the measures of Table 11. Then the effect of these rankings were measured by computing accuracy vs. number of features ordered by each ranking measure. The results are shown in Figure 31.

Measure	Ranking order
Bandwidth	Decreasing bandwidth of feature
Voltage SNR	Decreasing Voltage SNR of feature
Power SNR	Decreasing Power SNR of feature
V-P SNR	Decreasing difference between Voltage and Power SNR of the feature

Table 11. Various rankings of the feature set. The ranking order is for increasing feature number.

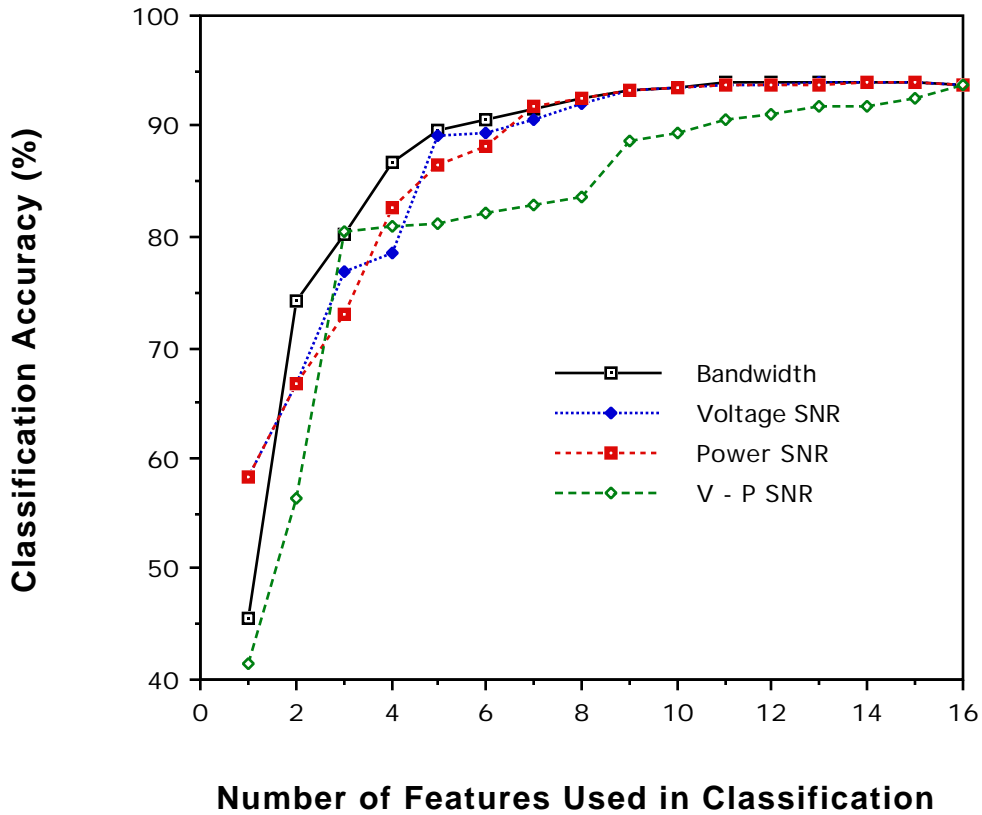


Figure 31. Classification accuracy vs. number of features for several different orderings of the feature set.

The ranking by bandwidth, as in Table 9, appears to have the best performance for small numbers of features. For one feature, the feature with the highest power SNR performed the best, and above 9 or 10 features, all rankings performed similarly.

An observation of these results is that the SNR of any individual feature is a poor predictor of that feature's importance when included in a multi-feature classification algorithm.

To obtain an overall measure of the SNR for a set of features, the method behind equations (6) and (7) was extended to combining the signals and noise from all wavelength bands contributing to the feature set.

To relate these combined SNR's to classification accuracy, a scatter plot was made of the SNR's for the various configurations used to produce Figures 22 through 27, and the resultant classification accuracies. This is shown in Figure 32 for the voltage and power feature SNR's.

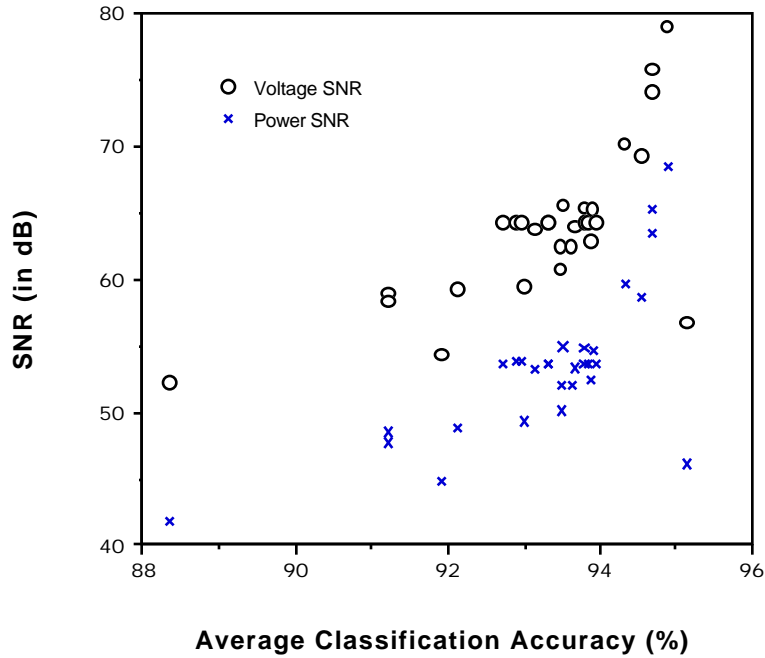


Figure 32. Classification accuracy vs. combined feature SNR.

Attempts to fit a linear or polynomial equation to these plots yielded a correlation coefficient of 0.71 for the best fit, that being a 3rd order polynomial. While there is a general relationship here between SNR and classification accuracy, they appear to be loosely correlated at best.

Also in this experiment, a multiclass implementation of the transformed Bhattacharyya separability measure was used to compute the effect of the parameters on separability. Equation (8) shows the two class transformed Bhattacharyya distance.

$$B_{ij} = 1 - e^{-1} \quad (8)$$

where,

$$= \frac{1}{8} (M_i - M_j)^T \frac{1}{2} (M_i + M_j)^{-1} (M_i - M_j) + \frac{1}{2} \log_e \frac{(|\Sigma_i + \Sigma_j|)^{1/2}}{(|\Sigma_i| |\Sigma_j|)^{1/2}}$$

Here, M_i is the feature mean vector of class i , while Σ_i is the feature covariance matrix of class i . The multiclass separability is computed using the apriori probability weighted sum over all classes i, j of the two class distances, as in equation (9).

$$\text{Separability} = \sum_{i=1}^I \sum_{j=1}^J p(i) p(j) B_{ij} \quad (9)$$

The plot of the classification accuracy vs. separability is shown in Figure 33. The r^2 value of the linear best fit line is 0.93. Thus, over this range of classification accuracy and separability there is a high correlation between the two.

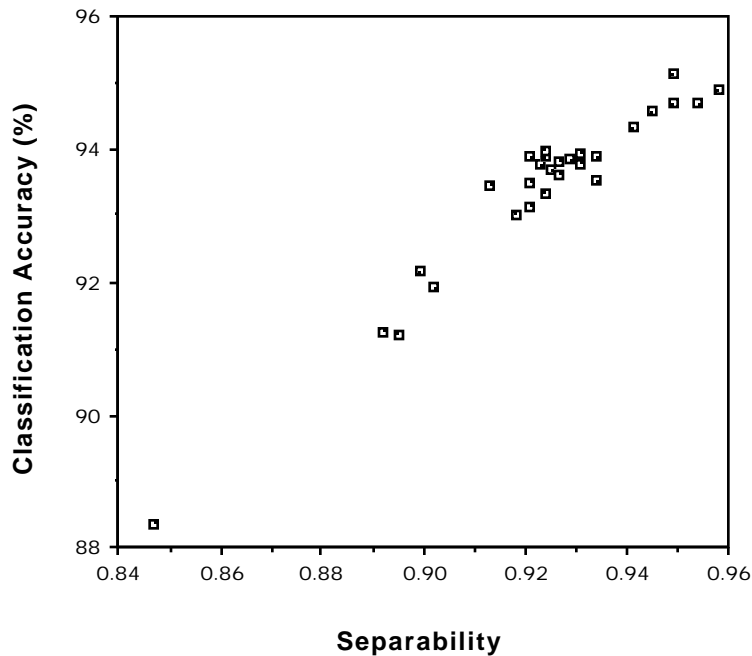


Figure 33. Classification accuracy vs. transformed Bhattacharyya distance.

A plot of the separability vs. SNR is shown in Figure 34. The best fit line has an $r^2 = 0.62$ for the voltage SNR and $r^2 = 0.63$ for the power SNR.

A tentative conclusion from these results is that while separability and classification accuracy are highly correlated, much less correlation exists between either the voltage or the power SNR and classification accuracy/separability.

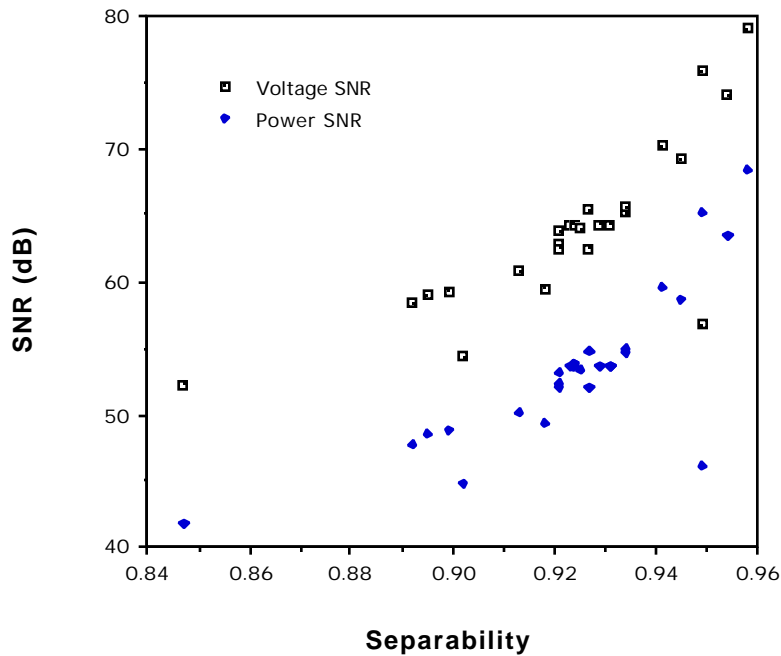


Figure 34. Transformed Bhattacharyya separability vs. combined feature SNR.

Several sets of six features (shown in Table 12) were used to evaluate their classification performance.

Feature	SFD	TM	WSNR	NSNR	SSFD	SSNR
1	0.42-0.66	0.45-0.52	0.40-0.70	0.51-0.56	0.59	0.54
2	0.66-0.84	0.52-0.60	0.77-0.90	0.81-0.86	0.75	0.84
3	0.70-0.92	0.63-0.69	1.00-1.10	1.02-1.07	0.81	1.04
4	1.48-1.64	0.76-0.90	1.15-1.30	1.20-1.25	1.56	1.11
5	1.98-2.20	1.45-1.75	1.50-1.74	1.59-1.64	2.10	1.61
6	2.20-2.40	2.08-2.35	1.97-2.40	2.16-2.21	2.30	2.19

Table 12. Wavelength bands combined for the various feature sets. The various feature sets are defined as SFD = Spectral Feature Design algorithm, TM = Landsat Thematic Mapper, WSNR = Wide Signal-to-Noise Ratio, NSNR = Narrow Signal-to-Noise Ratio, SSFD = Single band Spectral Feature, SSNR = Single band Signal-to-Noise Ratio.

The SNR features were chosen based upon regions of high SNR. These various sets were chosen to see how classification accuracy and combined signal-to-noise ratios compared. Figure 35 shows the combined SNR for the various feature sets, while Figure 36 shows the resultant classification accuracy for the baseline image used in this report.

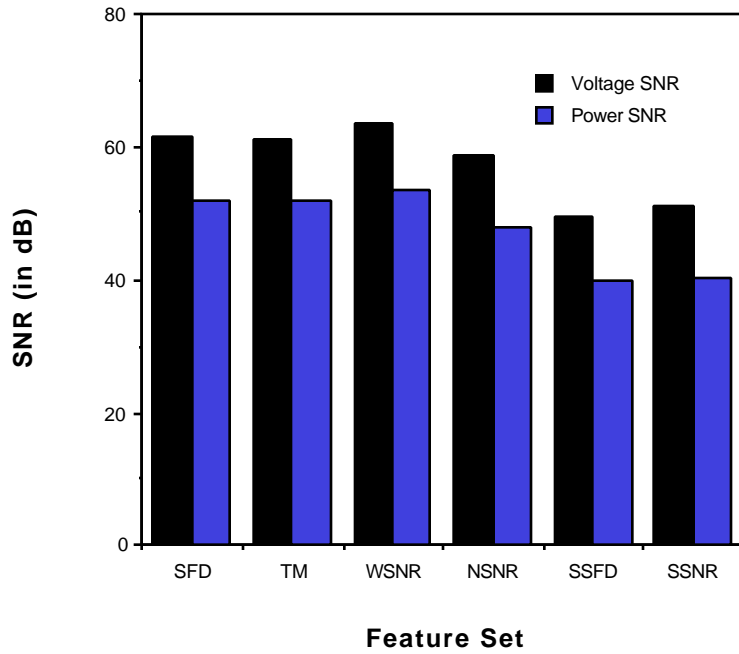


Figure 35. SNR's for the various feature sets.

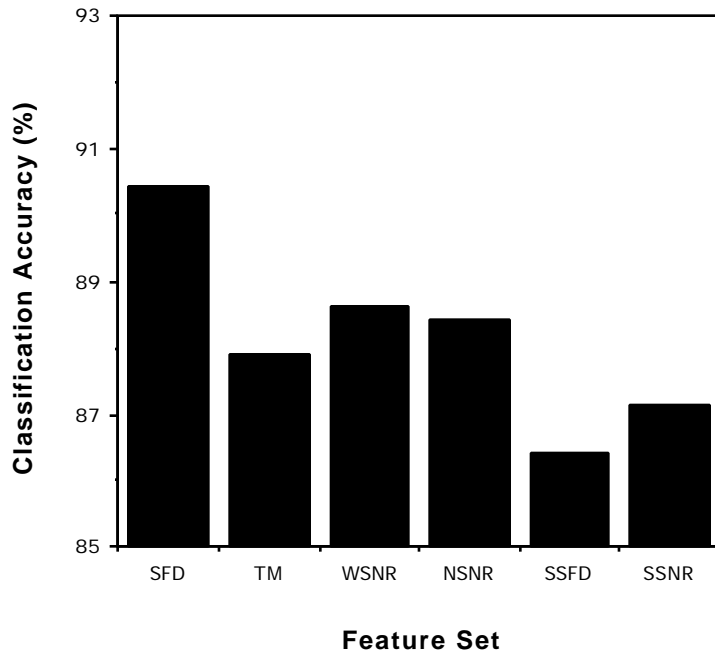


Figure 36. Classification accuracy for the various feature sets.

Clearly, the SFD features performed the best for this data set.

The robustness of the spectral feature design algorithm was then studied by comparing the accuracy of the various feature sets in classifying scenes created from other data sets than those from which the features were derived. Two other scenes were tested. One was created from reflectance data of three varieties of spring wheat. The second was from an artificial data set created from the covariance matrices of barley, pasture, and grain sorghum, with the same mean vector (that of barley). This was done to decrease the class separability and increase any difference in the classification accuracy due to the differing feature sets. When the original means were used all feature sets gave 99.9% accuracy. Tables 13 and 14 gives the specific fields from the LARS field data base combined for the two data sets.

Classes	Field	Number of Observations
Spring Wheat	118	13
	154	29
	199	28
	291	28
	292	16
		Total = 114
SW 1809	296	28
	303	58
		Total = 86
SW Mix	75	13
	281	55
		Total = 68

Table 13. Classes and fields used to compute statistics for the Spring Wheat test scene. The data is from Hand County, South Dakota, on July 26, 1978.

Classes	Field	Number of Observations
Barley	153	26
	231	21
	294	55
		Total = 102
Pasture	109	43
	194	45
	198	24
		Total = 112
Grain Sorghum	110	15
	256	51
	275	36
		Total = 102

Table 14. Classes and fields used to compute statistics for the Crops 3 test scene. The data is from Hand County, South Dakota, on July 26, 1978. In simulating the scene, the mean vector of the Barley class was used for all three classes.

Figure 37 shows the resulting accuracy for the various features and for the two test scenes. The crops 3 scene was tested for IMC = 1 and 8 to see the effect of increasing the SNR of the instrument on classification performance.

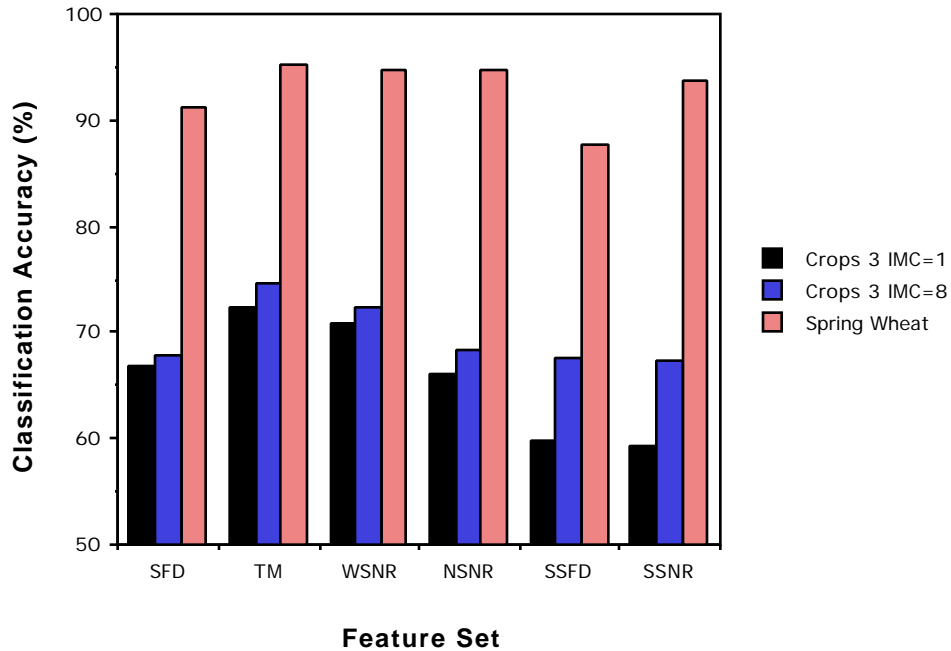


Figure 37. Classification accuracy for the various feature sets over two test scenes.

In all cases the features formed from the wavelengths used in the Landsat TM performed the best. The features derived from the high SNR regions also performed well. Compared to these two feature sets, the SFD feature set performed poorly.

This leads to a tentative conclusion that over varying scenes, the features derived from the reflectance of a different crop type, or scene, perform less well at classification than features derived from signal-to-noise regions of the instrument, or even the wavelength bands used in the Thematic Mapper. This is not surprising since the SFD procedure is intended to be case-specific; it is intended to provide features optimal for its design case, as compared to being optimal in the general case.

7. Summary and Conclusions

This report summarizes the current status of research into predicting the performance of the HIRIS instrument under varying system parameters, signal-to-noise conditions, and feature extraction methods.

Several tentative conclusions can be made.

- The current noise levels of the HIRIS instrument are adequate for use in classification studies.
- The radiometric resolution of 12 bits is well matched to the other sources of noise. At 8 bits, the quantization error becomes the dominant source of noise.
- The SNR of a feature obtained by combining bands is a poor predictor of the effectiveness of that feature alone in multivariate classification algorithms.
- The combined SNR of a feature set is a "loose" predictor of classification performance.
- Classification and separability are highly correlated.
- The features derived from the spectral feature design algorithm work well for a scene created from the statistics used in their design. However, they are not broadly optimum, and can be outperformed by more simply chosen feature sets.

Further work is necessary before etching these conclusions in stone.

8. References

- [1] Goetz, A.F.H., and M. Herring, "The High Resolution Imaging Spectrometer (HIRIS) for Eos," *IEEE Transactions on Geoscience and Remote Sensing*, Vol. GE-27, No. 2, pp. 136-144, March 1989.
- [2] Kerekes, J.P., and D.A. Landgrebe, "Simulation of Optical Remote Sensing Systems," submitted to the *IEEE Transactions on Geoscience and Remote Sensing*, for possible inclusion in the Special Issue on IGARSS '88 to be published in November 1989.
- [3] JPL, "High-Resolution Imaging Spectrometer (HIRIS): Phase A Final Report," JPL D-4782, Jet Propulsion Laboratory, California Institute of Technology, Pasadena, CA, November 1987. Also, data was obtained from viewgraphs used in a presentation by V. Wright of JPL on October 6, 1987 to the Imaging Spectrometer Science Advisory Group (ISSAG).
- [4] Markham, B.L., "The Landsat Sensors' Spatial Responses," *IEEE Transactions on Geoscience and Remote Sensing*, vol. GE-23, No. 6, pp. 864-875, November 1985.
- [5] Kneizys, F.X. et. al., "Users' Guide to LOWTRAN 7," AFGL-TR-88-0177, Air Force Geophysical Lab, Bedford, MA, August 1988.
- [6] Biehl, L.L., M.E. Bauer, B.F. Robinson, C.S.T. Daughtry, L.F. Silva, and D.E. Pitts, "A Crops and Soils Data Base for Scene Radiation Research," *Proceedings of the 8th International Symposium on Machine Processing of Remotely Sensed Data*, pp. 169-177, Purdue University, West Lafayette, IN, 1982.
- [7] Chen, C.-C., and D.A. Landgrebe, "A Spectral Feature Design System for High Dimensional Multispectral Data," *Proceedings of IGARSS '88 Symposium*, pp. 891-894, Edinburgh, Scotland, 13-16 September 1988. Also see Ph.D. thesis by C.-C. Thomas Chen, "Spectral Feature Design In High Dimensional Multispectral Data," School of Electrical Engineering, Purdue University, West Lafayette, IN, August 1988.